

University of Alberta

A metric for estimating perception of wound healing

by

Yaohua Wu



A thesis submitted to the Faculty of Graduate Studies and Research in partial fulfillment of the requirements for the degree of Master of Science

Department of Computing Science

Edmonton, Alberta
Fall 2004



Library and
Archives Canada

Bibliothèque et
Archives Canada

Published Heritage
Branch

Direction du
Patrimoine de l'édition

395 Wellington Street
Ottawa ON K1A 0N4
Canada

395, rue Wellington
Ottawa ON K1A 0N4
Canada

Your file *Votre référence*
ISBN: 0-612-95879-5
Our file *Notre référence*
ISBN: 0-612-95879-5

The author has granted a non-exclusive license allowing the Library and Archives Canada to reproduce, loan, distribute or sell copies of this thesis in microform, paper or electronic formats.

L'auteur a accordé une licence non exclusive permettant à la Bibliothèque et Archives Canada de reproduire, prêter, distribuer ou vendre des copies de cette thèse sous la forme de microfiche/film, de reproduction sur papier ou sur format électronique.

The author retains ownership of the copyright in this thesis. Neither the thesis nor substantial extracts from it may be printed or otherwise reproduced without the author's permission.

L'auteur conserve la propriété du droit d'auteur qui protège cette thèse. Ni la thèse ni des extraits substantiels de celle-ci ne doivent être imprimés ou autrement reproduits sans son autorisation.

In compliance with the Canadian Privacy Act some supporting forms may have been removed from this thesis.

Conformément à la loi canadienne sur la protection de la vie privée, quelques formulaires secondaires ont été enlevés de cette thèse.

While these forms may be included in the document page count, their removal does not represent any loss of content from the thesis.

Bien que ces formulaires aient inclus dans la pagination, il n'y aura aucun contenu manquant.

Canada

TABLE OF CONTENTS

Chapter 1.....	1
Chapter 2.....	6
Chapter 3.....	11
3.1 Wound size assessment.....	11
3.2 Wound border detection	17
3.3 Analysis of colors within the wound site.....	18
Chapter 4.....	22
Chapter 5.....	25
5.1 The preparation of the experiment	29
5.2 The background of the judges.....	31
5.3 The effect of the temporal sequencing factor.....	32
Chapter 6.....	33
6.1 Derivation of the healing function	36
6.2 Reliability of the observer evaluations	50
Chapter 7.....	53
bibliography.....	54

LIST OF FIGURES

<i>Number</i>	<i>Page</i>
Figure 1: Zoomage 3D dermatological scanner	2
Figure 2: Texture image of a scanned hand	3
Figure 3: Laser image of a scanned hand	3
Figure 4: 3D reconstruction from the laser and texture images of a scanned hand	4
Figure 5: A portion of a laser image	22
Figure 6: Intensity Histogram	24
Figure 7: The back of a human model	25
Figure 8: The small area on the back of a human model that is modified to mimic a wound	26
Figure 9: One of the laser images	27
Figure 10: The laser image that represents the best condition of the wound	28
Figure 11: The laser image that represents the worst condition of the wound	29
Figure 12: Interface of the Program	31
Figure 13: Best Fitting Line	38
Figure 14: Best Fitting Second-degree Curve	40
Figure 15: Best Fitting Exponential Curve	42
Figure 16: Best Fitting Exponential Curve with Restriction	43
Figure 17: Best Fitting Gaussian Curve	45
Figure 18: Best Fitting Gaussian Curve with Restriction	46
Figure 19: Healing Function <i>vs.</i> Group 1 Results	48
Figure 20: Healing function <i>vs.</i> Group 2 Results	49

INTRODUCTION

In previous studies of wound healing assessment, wound size measurement, wound border detection, and analysis of the colors within the wound site are commonly discussed. In this project, we attempt to retrieve some important parameters from the depth information of a wound that can provide strong indications of wound healing. We then propose an experimental strategy to derive a formula (healing function) by using those parameters to estimate the perceptual assessments of wound healing. In a previous study, Pan *et al.* [1] successfully proposed a similar experimental strategy to generate a model for estimating 3D perceptual quality.

In order to acquire the depth information on a wound, we use a simple technique based on the application of structured light. When scanning with a laser light, the depth information can be computed from the distortion along the detected location of reflected stripes [2]. In this project, we use the Zoomage3D dermatological scanner (Figure 1), from Zoomage Inc., to scan wounds. Based on structured light vision techniques, this dermatological scanner can be used to obtain 3D close-up images of a small area of the skin. It is able to generate two types of images: (1) the texture image, and (2) the laser image. The texture image

contains the texture of the scanning area, and the laser image contains the 3D depth information. By measuring the variations in each laser line, we can compute the depth of the corresponding area in the texture image [3][4]. We are then able to construct a 3D model of the scanned area by combining the two images. Figure 2 is a texture image of a scanned hand. Figure 3 is the corresponding laser image. A 3D model of the hand can be constructed by combining these two images (Figure 4). In this dissertation, however, we will focus on understanding how humans judge surface variations from laser patterns. Thus, we will not use the 3D reconstructed images.

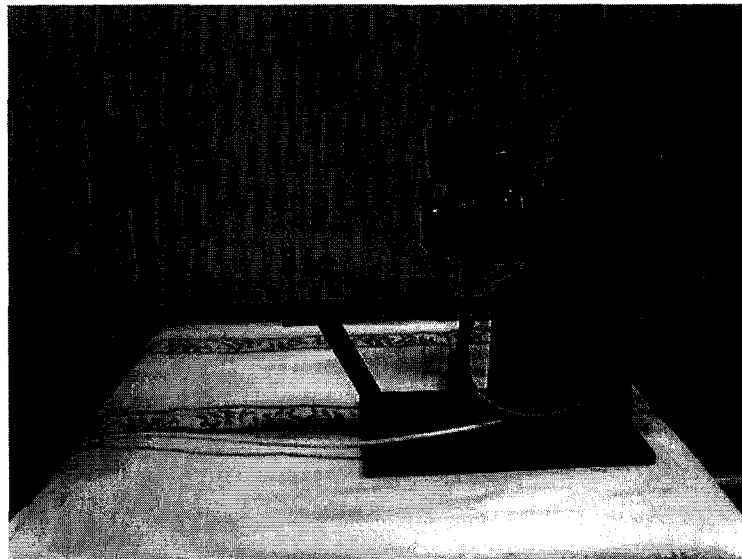


Figure 1: Zoomage 3D dermatological scanner



Figure 2: Texture image of a scanned hand



Figure 3: Laser image of a scanned hand

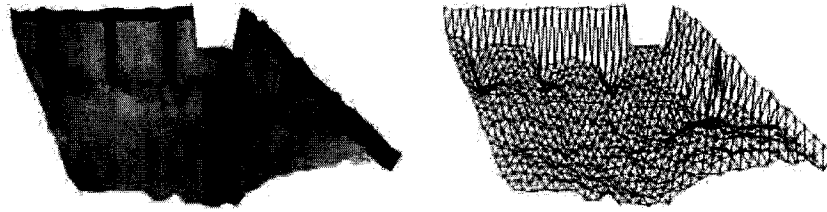


Figure 4: 3D reconstruction from the laser and texture images of a scanned hand

In this dissertation, we focus on the laser images since we are only interested in the depth information of a wound. In a laser image that is taken on a wound, the variations of the laser line segments reflect the depth information of the wound. In order to obtain the depth information of a wound, we need to distinguish the laser lines from the background, and retrieve the locations of necessary feature points from the laser lines, which represent the variations of the laser line segments. We then retrieve the relevant measurements that can give a strong indication of wound healing, and derive a metric according to the statistical data gathered from evaluation experiments. In our dissertation, once images are captured, computers can finish the process of registration, segmentation, and feature extraction automatically. Although we only use artificial wound for testing, the program in our dissertation is ready for use by physicians to test real wounds.

The remainder of this dissertation is organized as follows: Section 2 discusses background research. Section 3 reviews past work on wound healing assessment. Section 4 presents an adaptive approach for feature point extraction. Section 5 introduces the experimental environment. Section 6 describes the experimental results, derives the healing function and discusses the reliability of experimental data. Section 7 presents concluding remarks and future work.

Chapter 2

BACKGROUND

Computer vision performs an important role in computerized medical imaging applications. Its main objective is to extract useful information from image inputs that can later be used in these applications.

Image capturing is the very first step in computer vision. It can usually be divided into 2D and 3D image capturing. Since traditional 2D photographic methods have the disadvantage of projection errors arising from a naturally curved body surface being projected onto a flat image plane of a camera, 3D measurements are preferred in many medical imaging applications. Currently, the structured light vision technique is the most popular industrial vision technique for 3D image capturing. Compared to other techniques, structured light has the advantages of high accuracy and relatively low cost. A structured light vision system is usually composed of three basic components: a laser projector to project a laser beam onto objects, a CCD video camera able to capture images of the scene, and a computer that is connected to the camera and receives the images from it. The differences among these systems are usually based on the methods they use to form correspondences between camera pixels and locations in the projected pattern.

M^cIvor *et al.* [3] describe how to calibrate a structured light system. The system used in this paper is based on the use of pinhole optical models of the camera and projector comprising the system. The authors describe a method for determining the parameters of a 3×4 perspective transformation matrix (PTM) that is used for the transformation from 3D coordinates to 2D camera image plane coordinates. They show that the 3D data can be generated once the perspective transformation matrix for the camera and projector is given. Finally, they analyze the accuracy of their calibration model. It shows that there are several sources of errors existing in the model. For example, the linear pinhole optical model does not accurately model an actual physical lens system. They suggest that further investigations of ways to reduce errors should be considered in their model.

M^cIvor [4] presents an alternative approach to interpreting the data from a structured light system, and demonstrates that this approach results in more accurate 3D information. Instead of determining the position of the stripe in 3D space by finding the intersection of the projected light plane and the back-projection of the pixels forming the stripe's image, this approach focuses on the transition between stripes and equates them with planes projected in an ideal structured light system model. It projects only the transitions that are extracted from the images using standard sub-pixel techniques. This differs from the

more common method that uses sub-stripe interpolation to estimate the projector coordinate at image pixel centers, and then back-projects them to 3D points. This method demonstrates that 3D data can be simply achieved by interpolation in 3D between the 3D transition curves. The results show that 3D data acquired by this approach is more accurate and smoother locally.

DePiero *et al.* [2] discuss the design issues, calibration methodologies, and implementation schemes of a structured light vision system. They develop a structured light sensor called PRIME (the Profile Imaging Module) and use it as a model for their detailed discussion. The PRIME sensor is designed to scan continuously moving objects, and acquire vertical profiles of range data in real time by detecting the laser light that is projected onto the objects. 3D Cartesian range data of the moving object is acquired as the output of this sensor.

Guan *et al.* [5] utilize the traditional phase measuring profilometry (PMP) method [6] and present a methodology to combine multiple traditional PMP patterns into a single composite pattern, in order to recover the depth data of the moving or non-rigid object in real-time. The composite pattern technique has the benefit of capturing video sequences at the frame rate of the camera, and thus is well suited for real-time 3D reconstruction.

Liska *et al.* [7] present an adaptive 3D acquisition system, based on structured light, to reconstruct the viewable surface of an object completely. In this system, objects are placed on the turntable so that multiple views of the same object can be obtained. In order to reduce the light occlusions that occur because a ray of light cannot reach the complete surface, as well as the camera occlusions due to part of the surface being invisible to the camera, two laser lights are used in the system. In order to solve the problem of varying resolution in the surface facing the camera (which is due to the varying distance of object points from the rotational axis of the turntable), they introduce a next-view planning technique that estimates the next sensor position, depending on the object's surface structure. The next-view planning technique not only ensures they are able to obtain an optimal object surface resolution, but also reduces the computational effort in 3D surface reconstruction using a turntable.

Hall-Holt *et al.* [8] introduce a triangulation-based range scanning system for moving objects that returns dense range images in real time and derives the stripe boundary codes that allow range scanning of moving objects. In order to design a stripe boundary code, a color that is either black or white is needed to be assigned to each stripe at each point in time, so that each boundary has a unique code over the sequence of four frames. They implement the system and show that complete

models of rigid objects can be obtained rapidly and automatically, without the need for calibrated object motion.

Scharstein *et al.* [9] devise a method that can be used to automatically acquire high-complexity stereo image pairs with pixel-accurate correspondence information, using structured light. A pair of cameras and one or more laser light projectors that cast structured light sequence onto the scene are used in the method, which produces a pair of images. Each pixel in the pair of acquired images is uniquely labelled by using structured light, and correspondences between pixels in the two images can be established by finding matching label values. Two kinds of structured light are examined in this paper: binary gray codes and continuous sine waves. Experimental results show that the gray codes can provide them more reliable estimates of projector coordinates, due to the binary gray code's higher insensitivity. They demonstrate that their method is suitable for stereo algorithm evaluation.

REVIEW OF WOUND HEALING ASSESSMENT

With the development of computer technologies and image processing algorithms, more applications have been developed for wound healing assessment. In order to accurately and effectively assess the state of wounds, many applications have focused on wound size measurement, wound border detection, and analysis of the colors within the wound site.

3.1 Wound size assessment

Plassmann *et al.* [10] emphasize that accurate measurement of the wound size is vital for judging the healing process. They first introduce the difficulties of measuring the volume of wounds, and then discuss the performance of different volumetric measurement methods.

In their paper [10], the authors mention that there are five major difficulties when measuring the physical size of wounds. First, the definition of a wound's boundary is very subjective. Different human observers may estimate a totally different measurement of the wound boundaries for the same wound. Second, a wound is flexible: a slight movement may significantly change a wound's

appearance, and a change in the patient's position may significantly change a wound's appearance. Third, some part of the wound may be invisible to the measurement machines, due to the natural curvature of the human body. Fourth, volume definition of some wounds is difficult since it is hard to reconstruct the original healthy surface. Finally, wounds such as abdominal wounds that are located in areas with a thick covering layer of soft issue, may be difficult for volume measurement, since a cavity with a large volume may still be apparent even after the wound has healed completely.

The authors [10] then discuss the advantages and disadvantages of different wound volume measurement methods in terms of accuracy, precision, and practicability in a clinical environment. There are three methods mentioned in their work: the practice of filling the wound with saline, the production of alginate casts, and an image processing technique based on the structured light approach.

Volume measurement utilizing saline solution has been used for many years. This approach is straightforward [10]: the wound is covered with a thin layer of plastic material, such as semi-permeable film dressing that is transparent, elastic, and adhesive; then the cavity between the wound and the plastic material is filled in by injecting saline solution with a calibrated syringe. The amount of saline used to fill in the cavity is a direct measure of the wound's volume.

Volume measurement using casts is similar to volume measurement using saline solution. Instead of using saline, impression material is injected into the cavity of wounds. After the injected impression material is mixed with water and forms an elastic cast, the volume of wound can be determined by measuring the volume of the cast.

Volume measurement using computer vision, as discussed in this paper, is based on the structured light vision technique, which is similar to the structured light techniques discussed in section two.

Of the three methods discussed in the paper, the structured light-based method is the most precise. However, a computer operator for the structured light measurement method needs time for intensive training, and it is more expensive than the other two. The saline solution technique is easy to use and not expensive; however, the wound might absorb some of the saline, so it is inaccurate. In terms of real life, alginate casts are more preferable since they are more accurate than saline solution, easy to produce and inexpensive.

Plassmann *et al.* [11] introduce an instrument based on structured light to measure the wound areas and wound volumes. Before wound area and wound volume are calculated, the system operator must define the outline of the wound by tracing

its edge in the image without stripes, which is a semi-automated process. This process also introduces errors into the calculations. The original, healthy skin surface is reconstructed using cubic spline interpolation. The wound area is defined as the area of the reconstructed surface, and wound volume is defined as the sandwich between the measured surface and the reconstructed surface. Experimental results show that wound size cannot be measured when the wounds are very deep and very small.

Plassmann *et al.* [12] further design a non-invasive instrument based on the structured light vision technique for measuring wound areas and wound volumes. The instrument is named MAVIS – Measurement of Area and Volume Instrument System. Once an image is taken, an operator draws around the boundary of the wound with a mouse cursor in order to provide the system with information about the wound boundaries. This information is then used for further calculations of wound area and wound volume. As mentioned before, the authors define the wound volume as a sandwich between the measured surface and the original healthy skin surface, and use the cubic splines to interpolate the original healthy skin surface. In their experiments, they compare the performance of the instrument with three traditional wound measurement techniques: rulers (for length measurements), transparency tracings (for area measurements), and alginate casts (for volume measurements). The results show that the MAVIS instrument is more precise than all of the rest.

Jones *et al.* [13] introduce a new instrument to measure the dimensions and colors of skin ulcers and pressure sores. This instrument is based on the structured light vision technique. Since ulcers tend to heal from the base, rather than from the borders, volume measurements are helpful for the assessment of wound healing in ulcers. As mentioned previously, the structured light vision technique has the advantage of high accuracy in wound volume measurement. In order to solve the difficulty of original healthy surface reconstruction, the authors define the original healthy surface by a cubic spline interpolated between the surrounding areas of healthy skin and the existing ulcer surface. After images are taken, they explain the procedure for locating the center of the stripes, since that is the only information they need from the laser images when they calculate the area and volume of ulcer wounds. In their conclusion, they explain the factors that affect the precision of wound dimension measurement. The instrument introduced in the paper has been used in two hospital clinics on patients that suffer with skin ulcers, pressure sores, and other skin wounds.

Tsap *et al.* [14] present a computer vision approach for burn scar assessment. Scars usually indicate successful wound healing. They are different from normal skins in several ways, including color, texture, size, and shape. Burn scar assessment can be utilized as an important factor in wound healing assessment. In this paper, the difference of elasticity between scars and normal elastic skin is

utilized to assess burn scars. Normal elastic skin allows almost unrestricted body movements, but with scarring, skin material properties change, and skin movement is restricted. In the skin model, a grid pattern is drawn on the region of interest in order to observe the elasticity of the skin when pulled. The authors present a set of algorithms for objectively determining the elastic properties of burn scars relative to the surrounding normal skin area [14]. By determining the elastic properties of burn scars, the success of the healing process of wounds can also be defined.

Jones *et al.* [15] propose a semi-automated wound area measurement algorithm for measuring the area of leg ulcers. The algorithm adapts the active contour model that was first defined by Kass *et al.* [16]. Instead of using discrete points, the active contour model in this paper defines the contour as a piecewise parametric curve using cubic B-splines, and uses the mini-max principle to adaptively regularize the contour according to local conditions in the wound image. The experiments in this paper show that this contour model produces higher-precision leg ulcer area measurements when compared to measurements made by manual delineation, in most of the cases tested.

Krouskop *et al.* [17] present a non-contact wound measurement system that is based on structured light vision technique. They describe the device design of the system, which is similar to the structured light vision systems introduced in

Section Two. They provide details of image enhancement for the purpose of improving the precision of the system. They then introduce their wound area and wound volume calculation formulas. As mentioned before, in order to calculate wound volume, the original skin surface must be known, so a formula is presented for estimating the original skin surface. This formula assumes that the wounded part of the body is originally smooth and has only simple curvature in two orthogonal directions. In order to evaluate the precision of this system, plaster molds with spherical indentations are used to represent various wounds. The experimental results show that the wound measurement system is effective for measuring surface area and volume of wounds.

3.2 Wound border detection

Zhang *et al.* [18] introduce an automatic radial search technique for border detection on digitized skin tumor images. This radial search technique is based on the technique described by Golston *et al.* [19]. It first estimates the tumor center by performing the average luminance projection of a tumor image along its rows and columns. Then it starts two rounds of radial search based on the same tumor center. The first round is independent: the best-fit edge-detection method is applied for finding the reliable border points as seeds. The second round is dependent on the seed points from the first round, and the tumor border points are found, based on the simple prior knowledge that all the neighboring border points are close to each other. The experimental results show that the radial

search technique described in the paper improves on model images and clinical skin tumor images where the technique of Golston *et al.* [19] failed to find the correct border.

Schmid-Saugeon *et al.* [20] present a computer-aided diagnostic system for detecting pigmented skin lesion boundaries. The images are processed by the epiluminescence microscopy (ELM) technique, which use oil immersion to display the outer layer of the skin in order to reveal most of the pigmented structures by allowing the light to penetrate deeper into the skin. In order to prevent corruption of images, and facilitate the subsequent segmentation and feature quantification steps, a hair removal algorithm is introduced to remove hair from images before a lesion boundary detection algorithm is applied. In the lesion boundary algorithm, the authors combine a segmentation technique and a boundary detection technique to detect the lesion boundaries in the images. The experimental results show that the lesion boundaries obtained by this computer-aided diagnostic system generally are better than hand drawn boundaries obtained by each physician alone.

3.3 Analysis of colors within the wound site

Berriss *et al.* [21] review the recently published research into color image processing applied to skin wounds and lesions. There are two major applications in this field: assessments of skin wound or ulcer healings, and the diagnosis of

pigmented skin lesions. In wound healing assessments, wound border detection, wound size calculation, and analysis of the colors within the wound site are often very important. In diagnosis of pigmented skin lesions, image-processing techniques such as edge detection, segmentation, and object identification are often used for the purpose of analyzing the size, shape, irregularity, and color of the segmented lesion. The authors introduce the work of several research groups in the area of color image processing of wound healing, and emphasize that color image processing applied to skin wounds has advantages over human assessments of wounds, since it is difficult for humans to analyze and compare color images of wounds.

Hansen *et al.* [22] present a computer analysis of tissue color to assess the severity of wounds using color image processing. They use an animal wound model described by Kokate *et al.* [23] to simulate the human wound. The authors first attempt to develop a linear model that relates hue, saturation, and intensity to wound severity, but experimental results show that the model is not able to distinguish the severity of wounds. They then develop a non-linear model relates hue and saturation with wound severity. The results show that tissue hue can be used to distinguish wound severity. The authors believe that the major benefit of their system is its capability to accurately track the visual appearance of the wound site over time, and they have developed the methodology to repeatedly

quantify skin color, and then assess the utility of the technique to evaluate wounds.

Ercal *et al.* [24] use an artificial neural network to diagnose malignant melanoma from color skin images. They define a set of features that can be used to distinguish melanoma from three other types of (benign) tumors: dysplastic nevi, intradermal nevi and seborrheic keratoses. The features include color characteristics of tumors, tumor asymmetry, and border irregularity, and later experiments confirm that color characteristics of tumors play a crucial role in the diagnostic process [24]. The artificial neural network is a feedforward neural network with fourteen inputs, including the three features mentioned above, and one output that indicates whether the tumor is malignant melanoma or not, using the back-propagation rule. The authors show that a high level of accuracy in detecting malignant melanoma can be achieved in the experiments when using the artificial neural network.

Herbin *et al.* [25] propose a method of skin healing assessment using true color image processing techniques. They define two indices derived from image processing techniques: wound area index and wound color index. Wound area index is a surface area index that is based on automated delineation of wound. An optimal threshold value that is varied by interactively delineated wounds is used to decide whether a pixel is in the wound area or not. By combining the pixels

that are in the wound area, the wound area index is computed. Wound color index is the mean chromatic green in the wound. It appears to be more appropriate to follow up color variations induced by healing among a population of healthy volunteers [25]. Since the two indices are not directly related to each other, the authors propose both of these indices for the study of epidermal wound healing during clinical trials.

Bon *et al.* [26] define a healing function based on parameters obtained from digitized images of wounds. They first examine the sixteen candidate parameters that might be useful for wound healing assessment: the means of red, green, blue, luminance, chromatic red, green and blue, the standard deviations σ_R , σ_G , σ_B , σ_L , σ_r , σ_g , σ_b , and the number of minima and maxima [26]. Experimental analysis suggests that color homogeneity indicates healing better than does color, which indicates that the standard deviations of luminance and color are the most relevant parameters in defining the healing function. The authors then build the healing function based on the nine parameters: σ_R , σ_G , σ_B , σ_L , σ_r , σ_g , σ_b , and the number of minima and maxima. Experimental results show that the curve of healing function is close to the healing curve of patients.

ADAPTIVE APPROACH FOR FEATURE POINT EXTRACTION

We can acquire depth information of a wound by identifying the curvature changes of each (laser) line in a laser image taken of the wound. In order to identify curvature variations, one way is to extract some feature points from each laser line, as shown in Figure 5 (red points in the figure). The locations of the feature points give us information on the 3D surface changes from the laser lines.

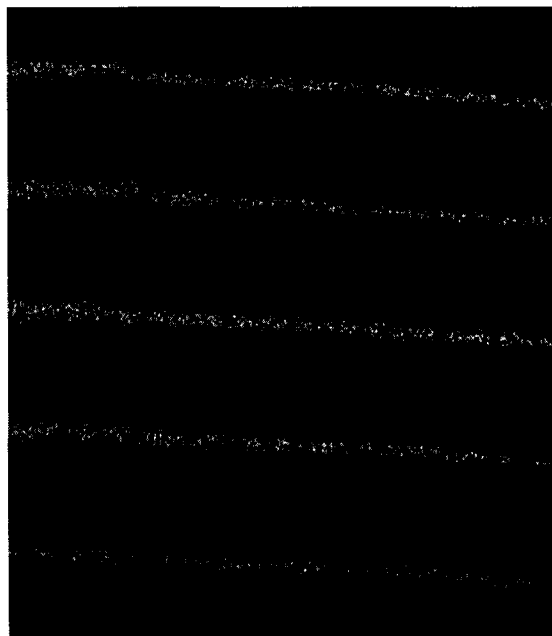


Figure 5: A portion of a laser image

A simple way to extract the feature points is to use a threshold to filter out all of the pixel points that do not lie on the laser lines. Since the pixel intensities vary for different laser images, we cannot apply a fixed threshold for all images. In addition, even in the same laser image, the pixel intensities may vary in different regions. Thus, instead of using global thresholding, adaptive thresholding is applied.

In our research, instead of retrieving all of the feature points along each laser line, we generally define a distance of N , and retrieve only the feature points N pixels apart along each laser line. The reason we do not retrieve all of the feature points is that we do not need all of the feature points in each laser line for the next step's computation. Since the laser lines will not be straight if the wound surface is not flat, it will be difficult to retrieve the feature points horizontally, line by line. Instead, we start from the bottom up to retrieve the feature points in each laser line vertically, as shown in Figure 5. Each time we begin to retrieve the feature points from the bottom up, we need to define a threshold, so that pixels that are not lying on the laser lines will be removed. Since there are clear separations between the laser lines and the background in each laser image, we use the intensity histogram (Figure 6) to decide the threshold. The x -axis represents the pixel intensities from 0 to 255, and the y -axis represents the occurrence of each intensity value. Generally, there are two clearly separated peaks in the histogram,

corresponding to the laser lines and the background. A suitable threshold for separating these two groups lies between the two peaks in the histogram. For example, in Figure 6 the threshold is 43.

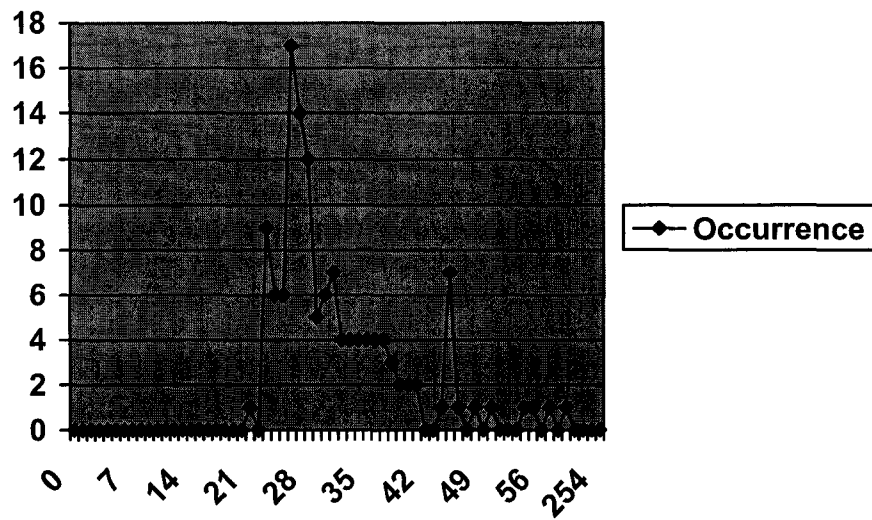


Figure 6: Intensity Histogram

Chapter 5

EXPERIMENTAL ENVIRONMENT

In our experiments, we chose a small area on the back of a human model to simulate a wound. Figure 7 shows the back of the human model. Figure 8 shows the small area on the back of the human model that is modified to mimic a wound.

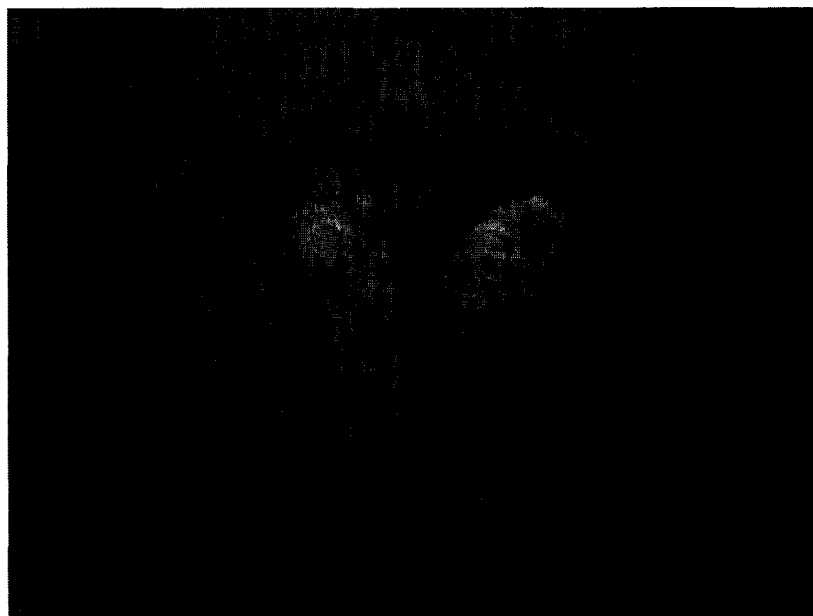


Figure 7: The back of a human model

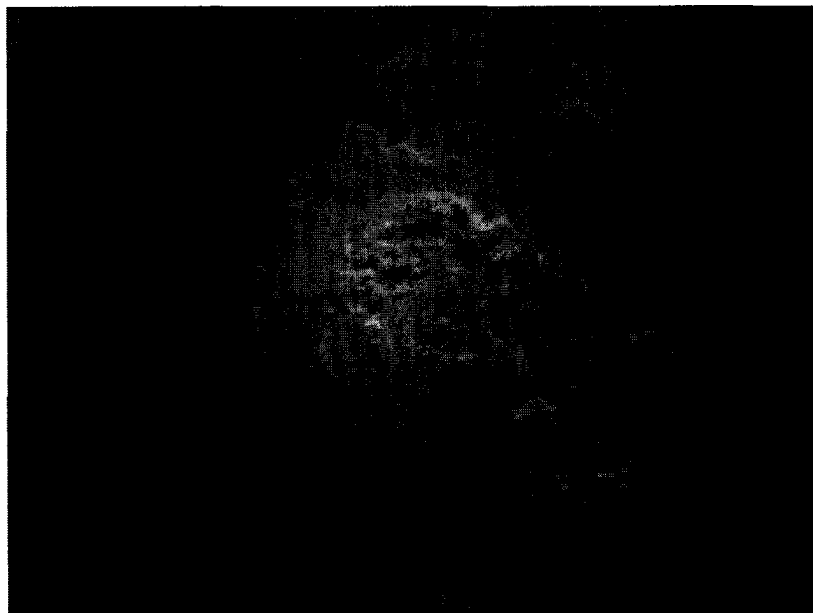


Figure 8: The small area on the back of a human model that is modified to mimic a wound

Plaster was added to the simulated wound in stages to simulate the process of the wound getting worse. We then removed the plaster in steps to simulate the process of the wound getting better. In total we took 11 images for the whole process. Each laser image contains 24 laser lines and has a resolution of 2558 * 3079 pixels, which is detailed enough for our experiments. Figure 9 shows one of the laser images. The first of the eleven laser images was taken when there was no plaster added to that area. So it was used to represent the best condition (the wound was healed). The seventh image was the last one taken during the process of incrementally adding plaster; *i.e.*, the seventh one represents the wound in its

worst condition. Figure 10 shows the image that represents the best condition of the wound. Figure 11 shows the image that represents the worst condition of the wound. Except for these two images, the others were subjectively evaluated.

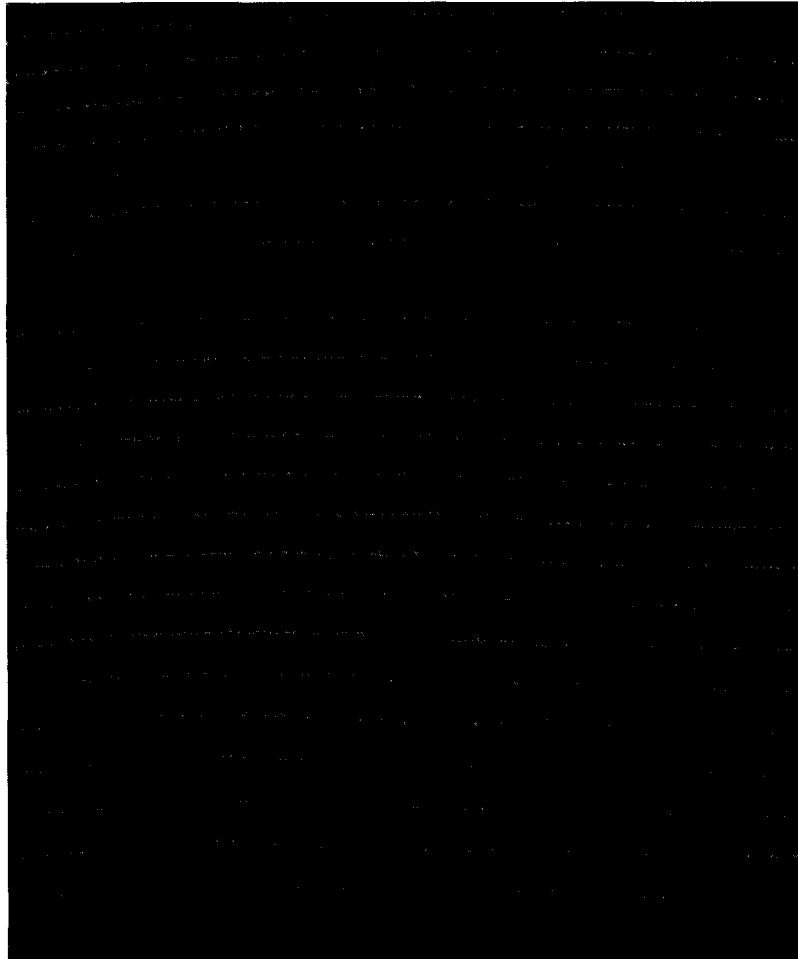


Figure 9: One of the laser images

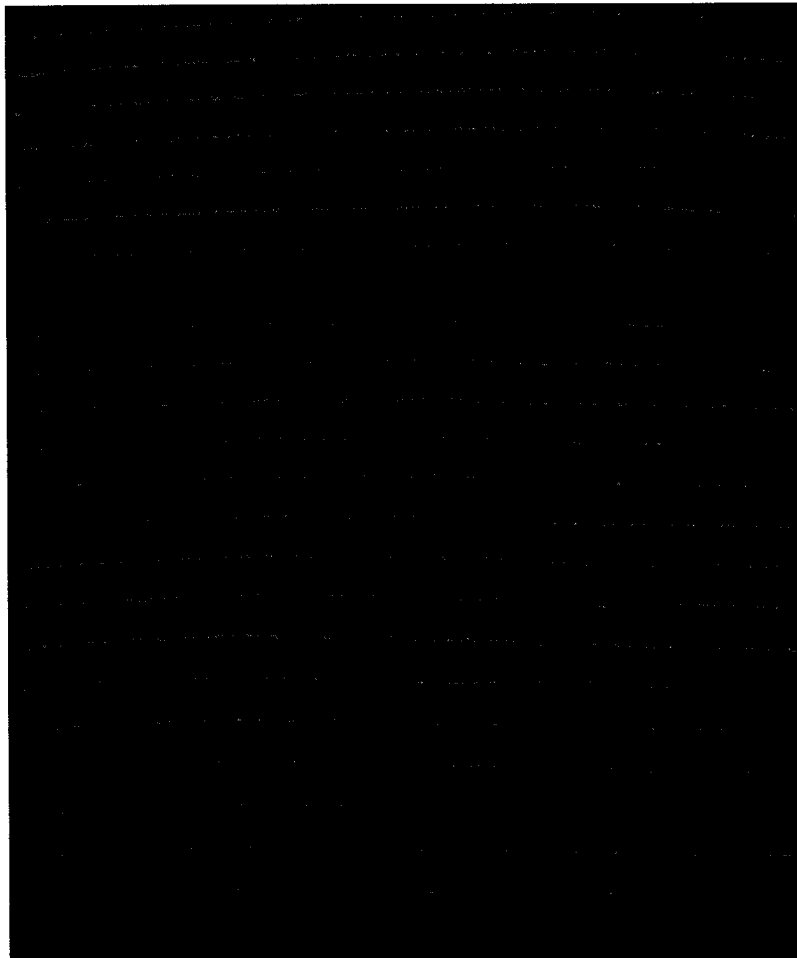


Figure 10: The laser image that represents the best condition of the wound

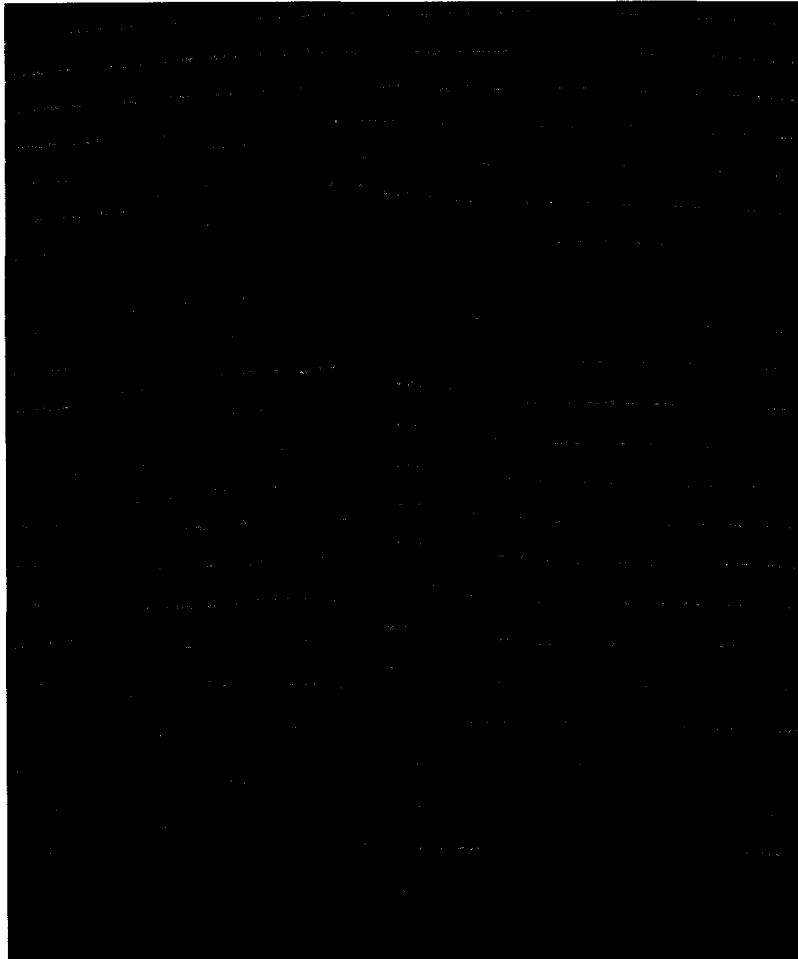


Figure 11: The laser image that represents the worst condition of the wound

5.1 The preparation of the experiment

In the experiment, there were 9 laser images used for evaluation. These laser images were evaluated by 20 judges, all of whom were graduate students from the Computing Science Department. To ensure the consistency of the experiment, all

of the evaluations were done on the same computer: a DELL desktop with 1.8GHZ processor, 512MB ram, Geforce3 video card, and a 21-inch Trinitron monitor. The resolution of the display was 1280 * 1024.

The judges were asked to rate the laser images by their assessment of the wound healing. Each laser image was expected to be assigned one of the following ratings: the wound is in a very good condition (5), the wound is in a good condition (4), the wound is in a fair condition (3), the wound is in a bad condition (2), the wound is in a very bad condition (1). Two more referential images were displayed side by side with the rating images for comparison; these two images were the first and seventh images as mentioned above. The first image was assigned a rating of 5 and placed at the right side, and the seventh was assigned a rating of 1 and placed at the left side. The judges were asked to compare the target (rating image) with the two referential images and assign it a rating between 1 and 5. Figure 12 shows the interface of the program that was used by the judges to evaluate the images.

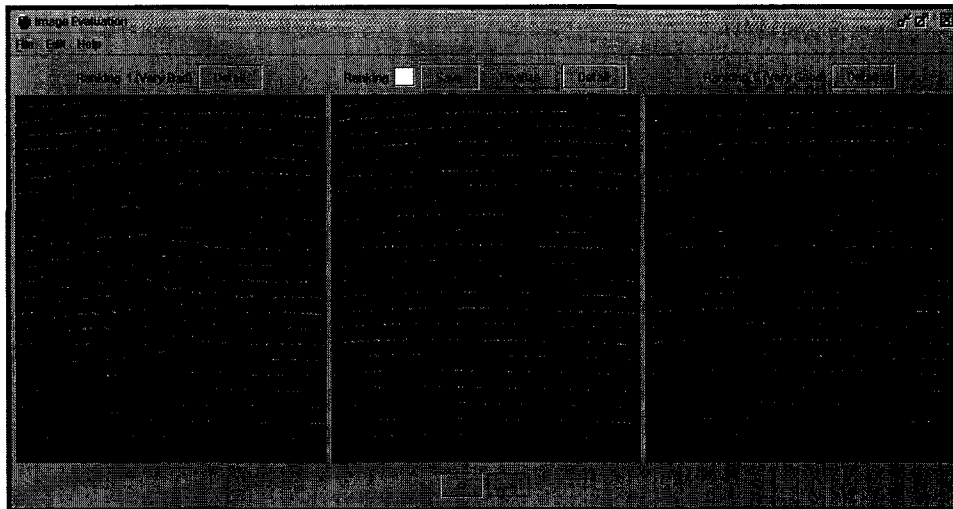


Figure 12: Interface of the Program

5.2 The background of the judges

In our experiment, the judges were expected to rate the laser images by their assessment of the wound healing. Thus they needed to know beforehand what laser images were and how to relate the laser images to the real wound.

We prepared an introduction for the judges before they took the evaluation. In the introduction, we explained how the laser images were generated and the connectivity between laser image and its corresponding texture image. A laser image (figure 3) and its corresponding texture image (figure 2) were also shown to the judges to give them impression how to relate laser images to real objects. One

reason that we chose all of the judges from the Computing Science Department is that they all had a thick background in computing science. All of the judges understood quickly. They would not start the evaluation until they were confident to make it.

5.3 The effect of the temporal sequencing factor

In order to avoid the effect of the temporal sequencing factor, the sequence of the 9 laser images was randomly generated so that no two judges shared the same sequence, and each judge made his/her decision independently. Only one object was displayed at a time to the judge.

Chapter 6

EXPERIMENTAL RESULTS AND DERIVATION OF A PERCEIVED HEALING FUNCTION

We divided the 20 judges into two groups, with each group containing 10 judges. The evaluation results from the first group are used for the derivation of the perceptual metric, and the evaluation results from the second group are used for estimating the reliability of the experimental results.

In each group, the rating of each image is the average of the evaluations from all the group members for that image. Table 1 shows the results of the image ratings by the first group. As mentioned above, the referential images (1 & 7) had ratings of 5 and 1, respectively.

Image list	Group 1 rating
Image 2	4.6
Image 3	4.4
Image 4	3
Image 5	2.7
Image 6	2
Image 8	2.1
Image 9	2.9
Image 10	3.8
Image 11	4.1

Table 1: Group 1 average ratings

Comparing the images with the experimental results from Group 1, when the laser images have more curved laser segments, the ratings of the laser images are smaller, indicating the wound is in a worse condition. As explained in Section 4, we use feature points to track the curve changes in a laser line. Here, we define a curve slope for each feature point. For each laser line, all of its feature points have an adjacent feature point at their left side except the leftmost feature point. In this experiment, therefore, we will ignore the leftmost feature points for each laser line. For all the other feature points in a laser line, we define the feature point's curve slope as:

$$\text{Curve Slope} = |(y_1 - y_0) / (x_1 - x_0)|$$

where (x_1, y_1) is the pixel location of the feature point, and (x_0, y_0) is the pixel location of its adjacent feature point on the left.

Thus we can calculate the average curve slopes of all the feature points in a laser image as shown in Table 2.

Image list	Group 1 rating	Average curve slope
Image 2	4.6	0.070
Image 3	4.4	0.078
Image 4	3	0.096
Image 5	2.7	0.106
Image 6	2	0.129
Image 8	2.1	0.115
Image 9	2.9	0.099
Image 10	3.8	0.092
Image 11	4.1	0.091

Table 2: Group 1 Average Ratings *vs.* Average Curve Slopes

It can be seen that when the average curve slope becomes larger, the image rating becomes smaller. Also, when the average curve slope is close to 0, the image

rating is close to 5, indicating that the wound has healed. When the average curve slope is close to ∞ , the image rating is close to 1, indicating that the wound is in a very bad condition.

6.1 Derivation of the healing function

As mentioned above, we use image rating to indicate the healing condition of the wound. When we define the healing function, we also use image rating to represent the healing condition. A suitable healing function should be the best fit of the data in table 2, and it has two restrictions: the maximum value of the image rating is 5 and the minimum value of the image rating is 1. Here we apply the least square method to retrieve the healing function.

The least square method assumes that the best fit curve of a given type curve has the minimal sum of the deviation squared (least square error) from a given set of data. Since we are not sure which type of curve will be the best fit, we will test several commonly used types below.

First, we will use a straight line to approximate the data in table 2. A straight line has the form of $y = a + bx$, where x represents the average curve slope, y represents the image rating, and a, b are the unknown parameters. The best fitting curve $f(x)$ has the least square error, i.e.,

$$\Pi = \sum_{i=1}^n [y_i - f(x_i)]^2 = \sum_{i=1}^n [y_i - (a + bx_i)]^2 = \min.$$

In order to obtain the least square error, the two unknown parameters a, b need to yield zero first derivatives.

$$\begin{cases} \frac{\partial \Pi}{\partial a} = 2 \sum_{i=1}^n [y_i - (a + bx_i)] = 0 \\ \frac{\partial \Pi}{\partial b} = 2 \sum_{i=1}^n x_i [y_i - (a + bx_i)] = 0 \end{cases}$$

After expanding and rearranging the above equations, the two unknown parameters a, b can be obtained.

$$\left\{ \begin{array}{l} a = \frac{\left(\sum_{i=1}^n y \right) \left(\sum_{i=1}^n x^2 \right) - \left(\sum_{i=1}^n x \right) \left(\sum_{i=1}^n xy \right)}{\left(n \sum_{i=1}^n x^2 \right) - \left(\sum_{i=1}^n x \right)^2} \\ b = \frac{\left(n \sum_{i=1}^n xy \right) - \left(\sum_{i=1}^n x \right) \left(\sum_{i=1}^n y \right)}{\left(n \sum_{i=1}^n x^2 \right) - \left(\sum_{i=1}^n x \right)^2} \end{array} \right.$$

After calculation, we have the best fitting line:

$$\left\{ \begin{array}{l} y = 5, \quad 0 \leq x \leq 0.02696 \\ y = 5.685 - 25.405x, \quad 0.02696 < x \leq 0.18441 \\ y = 1, \quad x > 0.18441 \end{array} \right.$$

Figure 13 shows the graph of the best fitting line.

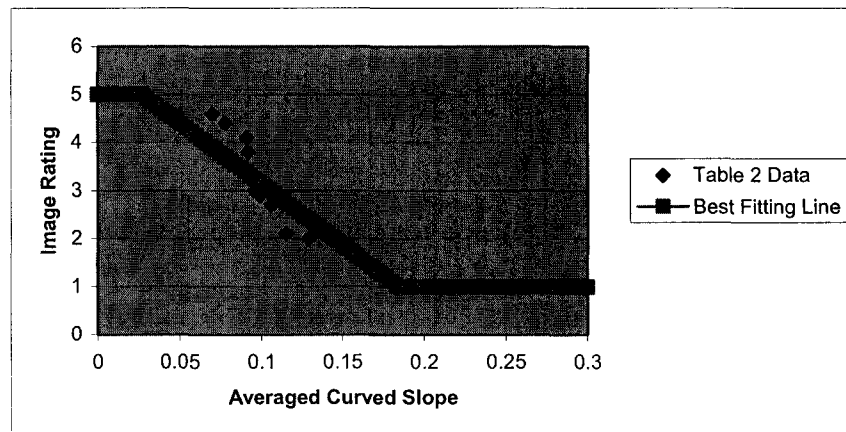


Figure 13: Best Fitting Line

Second, we will use a second-degree curve $y = a + bx + cx^2$ to approximate the data in table 2, where x represents the average curve slope, y represents the image rating, a , b and c are the unknown parameters. Again, the best fitting curve $f(x)$ has the least square error, i.e.,

$$\Pi = \sum_{i=1}^n [y_i - f(x_i)]^2 = \sum_{i=1}^n [y_i - (a + bx_i + cx_i^2)]^2 = \min.$$

In order to obtain the least square error, the unknown parameters a , b , and c need to yield zero first derivatives.

$$\begin{cases} \frac{\partial \Pi}{\partial a} = 2 \sum_{i=1}^n [y_i - (a + bx_i + cx_i^2)] = 0 \\ \frac{\partial \Pi}{\partial b} = 2 \sum_{i=1}^n x_i [y_i - (a + bx_i + cx_i^2)] = 0 \\ \frac{\partial \Pi}{\partial c} = 2 \sum_{i=1}^n x_i^2 [y_i - (a + bx_i + cx_i^2)] = 0 \end{cases}$$

After rearranging the above equations, we can calculate the three unknown parameters. The values of the three parameters are: $a=5.05866$, $b=13.16885$, $c=313.29648$. So the best fitting second-degree curve is:

$$\begin{cases} y = 5, & 0 \leq x \leq 0.04610 \\ y = 5.05866 + 13.16885x - 313.29648, & 0.04610 < x \leq 0.13676 \\ y = 1, & x > 0.13676 \end{cases}$$

Figure 14 shows the graph of the best fitting second-degree curve.

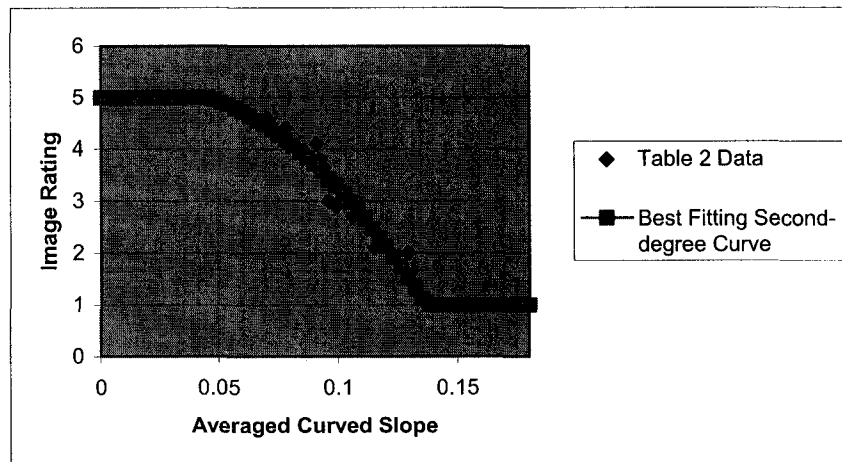


Figure 14: Best Fitting Second-degree Curve

Now we use an exponential curve $y = Ar^x$ to approximate the data in table 2, where x represents the average curve slope, y represents the image rating, r and A are the unknown parameters.

Before we start to look for the best fitting curve $f(x)$, we need to simplify the format of the exponential curve first. First, we apply the logarithm operation on both sides of the formula,

$$\log(y) = \log(A) + x \log(r)$$

Second, replace $\log(y)$ with y' , $\log(A)$ with a , $\log(r)$ with b , so that we have a new format of the formula, which is exactly a format of a line,

$$y' = a + bx$$

Following the steps above when we calculate the best fitting line, we can obtain the values of a and b , then we can obtain the values of A and r . The best fitting exponential curve is:

$$\begin{cases} y = 5, & 0 \leq x \leq 0.03198 \\ y = 6.34559 \times (0.00058)^x, & 0.03198 < x \leq 0.24794 \\ y = 1, & x > 0.24794 \end{cases}$$

Figure 15 shows the graph of the best fitting exponential curve.

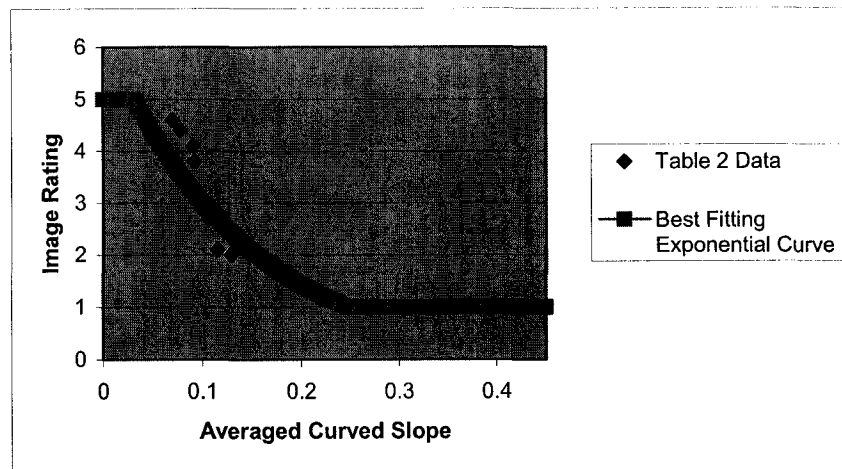


Figure 15: Best Fitting Exponential Curve

When we compute the best fitting exponential curve above, we don't consider the restriction that the minimum value of the image rating is 1 at the beginning. It is reasonable to put the restriction under consideration. In order to make sure that the value of y will not be smaller than 1, we use another exponential curve

$y = Ar^x + 1$ to approximate the data in table 2, where x represents the

average curve slope, y represents the image rating, r and A are the unknown parameters.

Following the similar steps when calculating the best fitting exponential curve, we can have the following best fitting exponential curve with restriction:

$$\begin{cases} y = 5, & 0 \leq x \leq 0.03426 \\ y = 5.82378 \times (1.7274 \times 10^{-5})^x + 1, & x > 0.03426 \end{cases}$$

Figure 16 shows the graph of the best fitting exponential curve with restriction.

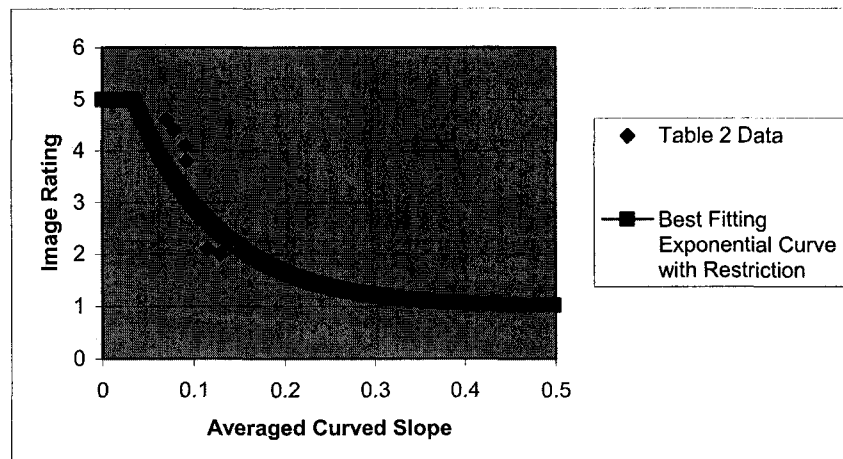


Figure 16: Best Fitting Exponential Curve with Restriction

Last, we will use a Gaussian curve $y = k_0 e^{-(x-k_1)^2 / k_2}$ to approximate the data in table 2, where x represents the average curve slope, y represents the image rating, k_0 , k_1 and k_2 are the unknown parameters.

Again, we need to simplify the format of the Gaussian curve first. Apply the logarithm operation to both sides:

$$\log(y) = \log(k_0) + \log\left(e^{-(x-k_1)^2 / k_2}\right)$$

We can further extend the above formula, and have:

$$\log(y) = \log(k_0) - (x^2 - 2k_1x + k_1^2) / k_2$$

Now we replace $1/k_2$ with c' , and have:

$$\log(y) = -c'x^2 + 2c'k_1x + \log(k_0) - c'k_1^2$$

Replace $\log(y)$ with y' , $-c'$ with c , $2c'k_1$ with b ,

$\log(k_0) - c'k_1^2$ with a , so that we have a format of a second-degree curve:

$$y' = a + bx + cx^2$$

Following the steps above when we calculate the besting fitting second-degree curve, we can obtain the values of the unknown parameters, then we can obtain the best fitting Gaussian curve:

$$\begin{cases} y = 5, & 0 \leq x \leq 0.05924 \\ y = 5.55498e^{-(x-0.02882)^2/0.00879}, & 0.05924 < x \leq 0.15159 \\ y = 1, & x > 0.15159 \end{cases}$$

Figure 17 shows the graph of the best fitting Gaussian curve.

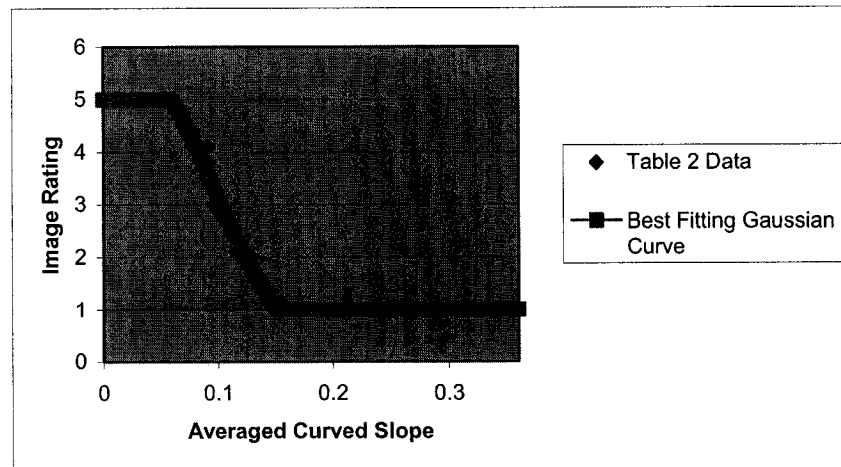


Figure 17: Best Fitting Gaussian Curve

When we use the Gaussian curve to approximate the data in table 2, we don't put into consideration that the minimum value of the image rating is 1. In order to make sure that the value of y will not be smaller than 1, we use another Gaussian

curve $y = k_0 e^{-(x-k_1)^2 / k_2} + 1$ to approximate the data in table 2, where x represents the average curve slope, y represents the image rating, k_0 , k_1 and k_2 are the unknown parameters.

Following the similar steps above, we can obtain the best fitting Gaussian curve with restriction:

$$\begin{cases} y = 5, & 0 \leq x \leq 0.06397 \\ y = 4.8469e^{-(x-0.03156)^2 / 0.00547} + 1, & x > 0.06397 \end{cases}$$

Figure 18 shows the graph of the best fitting Gaussian curve with restriction.

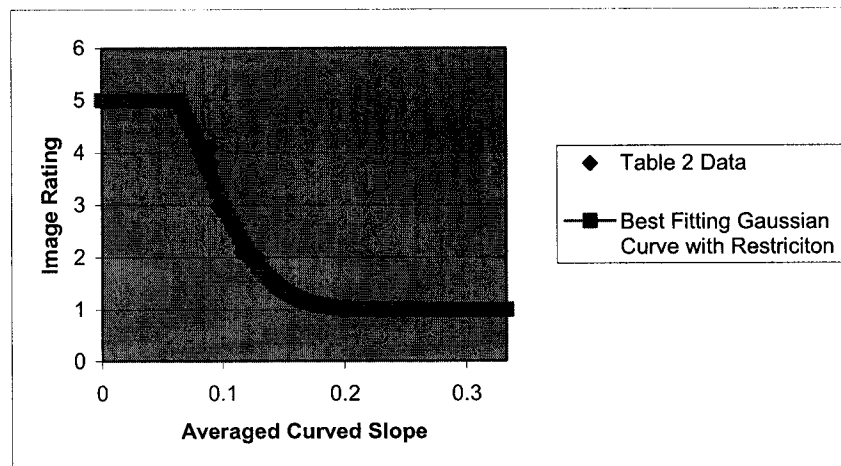


Figure 18: Best Fitting Gaussian Curve with Restriction

The curve that has the minimal sum of the deviation squared (least square error) from the data in table 2 is considered as the best fitting curve. Table 3 shows the sum of the deviation squared between different types of best fitting curves. We can see that the best fitting Gaussian curve with restriction has the minimum sum of the deviation squared from the data in table 2, so it is the best fitting curve here.

Curve	Sum of the deviation squared
Best Fitting Line	2.52395
Best Fitting Second-degree Curve	1.01156
Best Fitting Exponential Curve	3.15233
Best Fitting Exponential Curve with Restriction	3.52028
Best Fitting Gaussian Curve	0.70695
Best Fitting Gaussian Curve with Restriction	0.64660

Table 3: The sum of the deviation squared between different types of best fitting curve

Thus the healing function is:

$$\begin{cases} y = 5, & 0 \leq x \leq 0.06397 \\ y = 4.8469e^{-(x-0.03156)^2 / 0.00547} + 1, & x > 0.06397 \end{cases}$$

Figure 19 shows the healing function curve with respect to group 1 results. We will use this healing function as an approximation of the subjective healing evaluations.

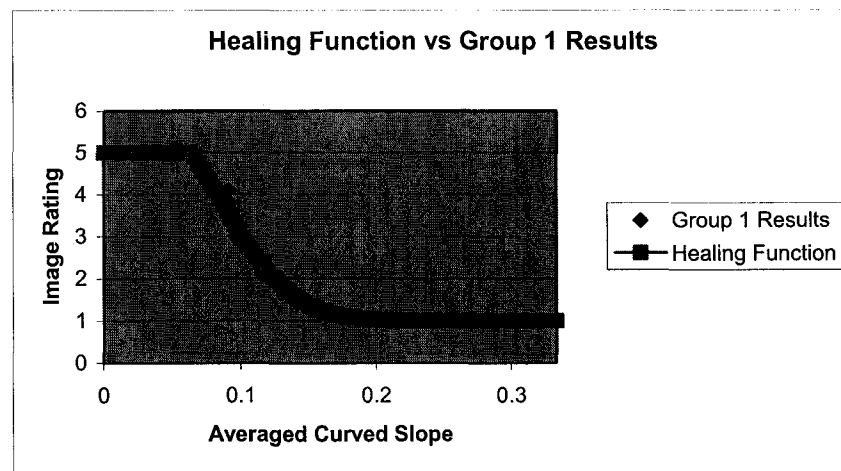


Figure 19: Healing Function *vs.* Group 1 Results

We also use Group 2 results to test whether the healing function is reliable. Table 4 shows group 2 results. Figure 20 shows the healing function with respect to group 2 results. It can be seen that all the sample points from group 2 are distributed close to the healing function curve, similar to group 1.

Image list	Group 2 rating	Average curve slope
Image 2	4.8	0.070
Image 3	4.4	0.078
Image 4	3.1	0.096
Image 5	2.7	0.106
Image 6	1.7	0.129
Image 8	2.3	0.115
Image 9	3	0.099
Image 10	3.9	0.092
Image 11	4.2	0.091

Table 4: Group 2 Average Ratings *vs.* Average Curve Slopes

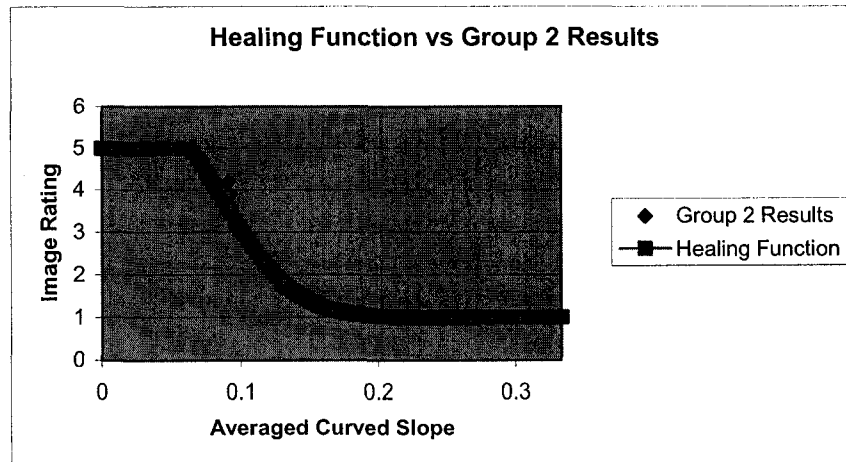


Figure 20: Healing function *vs.* Group 2 Results

6.2 Reliability of the observer evaluations

The derivation of our healing function is based on perceptual evaluation results. Therefore, it is important to discuss the reliability of our perceptual evaluations. Guilford [27] states that reliability increases with the number of judges (observers), and “reliability rating of 0.90 can be obtained with 10 to 50 judges.” In our experiment, we have 10 judges in each group. In order to make sure that they have similar educational and professional backgrounds, we chose only graduate students in Computing Science. As mentioned in Guilford’s book, “the reliability of measurements is determined by a self-correlation; repeated sets of measurements are correlated with each other.” However, it is a difficult and time-consuming task to form groups for self-correlation, since an additional group of judges for self-correlation must have comparable judging behaviour. This requires conducting extensive psychological behaviour tracking over time, which is beyond the scope of our preliminary study. Instead of computing correlation between similar judges, we will consider correlations of the average evaluations of the two groups of judges. Table 5 displays the evaluation results of the images of the two groups.

Image list	Group 1 rating	Group 2 rating
Image 2	4.6	4.8
Image 3	4.4	4.4
Image 4	3	3.1
Image 5	2.7	2.7
Image 6	2	1.7
Image 8	2.1	2.3
Image 9	2.9	3
Image 10	3.8	3.9
Image 11	4.1	4.2

Table 5: Group 1 Average Ratings *vs.* Group 2 Average Ratings

In order to quantify the strength of the linear association between the two groups, we need to calculate the correlation coefficient. Given the data in table 5, the correlation coefficient is calculated by:

$$r = \frac{1}{n-1} \sum \left(\frac{x - \bar{x}}{S_x} \right) \left(\frac{y - \bar{y}}{S_y} \right)$$

Where n is the number of the images tested, which is 9 here, x represents the image ratings in group 1, \bar{x} represents the average value of image ratings in group 1, S_x represents the standard deviation of image ratings in group 1, y

represents the image ratings in group 2, \bar{Y} represents the average value of image ratings in group 2, and S_y represents the standard deviation of image ratings in group 2.

The correlation between the two groups is 0.881, which means there is a fair positive correlation. Although we did not follow the psychometric guidelines strictly, this still indicates that there is a strong association between repeated sets of measurements of a “similar” group of judges, which leads us to believe that the reliability of our study should be fairly high, possibly around 0.90.

Guilford also mentioned that: “ranking becomes difficult and irksome when there are more than 30 to 40 stimuli.” In our experiment, only 3 stimuli (images) were shown at a time to the user, and the total number of stimuli per judge was 9. We thus believe that we used an appropriate number of stimuli.

CONCLUSIONS AND FUTURE WORK

In this dissertation, we proposed an experimental strategy for generating a healing function for wound healing assessment. We described how to extract relevant parameters according to the statistical data acquired from the perceptual experiment, and we applied the least squares method to generate a healing function that is based on the extracted parameters. The experimental results show that the perceptual evaluation results are reasonably close to the curve of our healing function. We also discussed the reliability of the perceptual evaluation results and showed that the reliability is fairly high.

For now we only concern the depth information of wounds in our healing function, in the future, we hope we can extend our healing function so that wound size, wound border and wound color are also considered when we build the healing function. Although we only use artificial wound to test our approach, it is ready for use by the physicians on the real medical images.

BIBLIOGRAPHY

- [1] Y. Pan, I. Cheng, and A. Basu, "Quantitative metric for subjective 3D quality evaluation," to appear in IEEE Transactions on Multimedia, 2004.
- [2] F.W. DePiero, and M.M. Trivedi, "3-D computer vision using structured light: design, calibration and implementation issues," Advances in computers, Vol. 43, pp. 243-278, 1996.
- [3] A.M. McIvor, and R.J. Valkenburg, "Calibrating a structured light system," in Image & Vision Computing New Zealand, Industrial Research Limited, pp. 167-172, 1995.
- [4] A.M. McIvor, "An alternative interpretation of structured light system data," DICTA/IVCNZ97, Massey university, New Zealand, pp. 41-46, 1997.
- [5] C. Guan, L.G. Hassebrook, and D.L. Lau, "Composite structured light pattern for three-dimensional video," Optics Express, Vol. 11, No. 5, pp. 406-417, 2003.
- [6] V. Srinivasan, H.C. Liu, and M. Halioua, "Automated phase measuring profilometry: a phase mapping approach," Applied Optics, Vol. 24, pp. 185-188, 1985.
- [7] C. Liska, and R. Sablatnig, "Adaptive 3D acquisition using laser light," Proc. of Czech Pattern Recognition Workshop, pp. 111-116, 2000.
- [8] O. Hall-Holt, and S. Rusinkiewicz, "Stripe boundary codes for real-time structured-light range scanning of moving objects," Eighth International Conference on Computer Vision (ICCV), Vol. 2, pp. 359-366, 2001.

- [9] D. Scharstein, and R. Szeliski, "High-accuracy stereo depth maps using structured light," IEEE Computer Society Conference on Computer Vision and Pattern Recognition, Vol. 1, pp. 195-202, 2003.
- [10] P. Plassmann, K.G. Harding, and J.M. Melhuish, "Methods of measuring wound size – a comparative study," Wounds, Vol. 6, No. 2, pp. 54-61, 1994.
- [11] P. Plassmann, B.F. Jones, and E.F.J. Ring, "A structured light system for measuring wounds," Photogrammetric Record, Vol. 15, No. 86, pp. 197-204, 1995.
- [12] P. Plassmann, and T.D. Jones, "MAVIS: a non-invasive instrument to measure area and volume of wounds," submitted by invitation to Medical Engineering & Physics, Vol. 20, pp. 325-331, 1998.
- [13] B.F. Jones, and P. Plassmann, "An instrument to measure the dimensions of skin wounds," IEEE Transactions on Biomedical Engineering, Vol. 42, No. 5, pp. 464-470, 1995.
- [14] L.V. Tsap, D.B. Goldgof, S. Sarkar, and P.S. Powers, "A vision-based technique for objective assessment of burn scars," IEEE Transactions on Medical Imaging, Vol. 17, No. 4, pp. 620-633, 1998.
- [15] T.D. Jones, and P. Plassmann, "An active contour model for measuring the area of leg ulcers," IEEE Transactions on Medical Imaging, Vol. 19, No. 12, pp. 1202-1210, 2000.
- [16] M. Kass, A.P. Witkin, and D. Terzopoulos, "Snakes: Active contour models," in Proc. 1st Int. Conf. Computer Vision, pp. 259-268, 1987.

- [17] T.A. Krouskop, R. Baker, and M.S. Wilson, "A noncontact wound measurement system," *Journal of Rehabilitation Research and Development*, Vol. 39, No. 3, pp. 337-346, 2002.
- [18] Z. Zhang, W.V. Stoecker, and R.H. Moss, "Border detection on digitized skin tumor images," *IEEE Transactions on Medical Imaging*, Vol.19, No. 11, pp. 1128-1143, 2000.
- [19] J.E. Golston, R.H. Moss, and W.V. Stoecker, "Boundary detection in skin tumor images: an overall approach and a radial search algorithm," *Pattern Recognition*, Vol. 23, No. 11, pp. 1235-1247, 1990.
- [20] P. Schmid-Saugeon, J. Guillod, and J. Thiran, "Towards a computer-aided diagnosis system for pigmented skin lesions," *Computerized Medical Imaging and Graphics*, Vol. 27, No. 1, pp. 65-78, 2003.
- [21] W.P. Berriss, and S.J. Sangwine, "Automatic quantitative analysis of healing skin wounds using colour digital image processing," *World Wide Wounds*, <http://www.worldwidewounds.com/1997/july/Berris/Berris.html> (online journal), 1997.
- [22] G.L. Hansen, E.M. Sparrow, J.Y. Kokate, K.J. Leland, and P.A. Iaizzo, "Wound status evaluation using color image processing," *IEEE Transactions on Medical Imaging*, Vol. 16, No. 1, pp. 78-86, 1997.
- [23] J.Y. Kokate, K.J. Leland, A.M. Held, G.L. Hansen, G.L. Kveen, B.A. Johnson, M.S. Wilke, E.M. Sparrow, and P.A. Iaizzo, "Temperature-modulated

pressure ulcers: A porcine model,” Arch Phys Med Rehab, Vol. 76, pp. 666-674, 1995.

[24] F. Ercal, W.V. Stoecker, H. Lee, and R.H.Moss, “Neural network diagnosis of malignant melanoma from color images,” IEEE Transactions on Biomedical Engineering, Vol. 41, No. 9, pp. 837-845, 1994.

[25] M. Herbin, F.X. Bon, A. Venot, F. Jeanlouis, M.L. Dubertret, L. Dubertret, and G. Strauch, “Assessment of healing kinetics through true color image processing,” IEEE Transactions on Medical Imaging, Vol. 12, No. 1, pp. 39-43, 1993.

[26] F.X. Bon, E. Briand, S. Guichard, B. Couturaud, M. Revol, J. Servant, and L. Dubertret, “Quantitative and kinetic evolution of wound healing through image analysis,” IEEE Transactions on Medical Imaging, Vol. 19, No. 17, pp. 767-772, 2000.

[27] J.P. Guilford, “Psychometric methods,” McGraw-Hill Book Company Inc., 1936